analytical chemistry

pubs.acs.org/ac Article

Charge Mapping of *Pseudomonas aeruginosa* Using a Hopping Mode Scanning Ion Conductance Microscopy Technique

Jake Rabinowitz,[§] Andreas J. W. Hartel,[§] Hannah Dayton, Jason D. Fabbri, Jeanyoung Jo, Lars E. P. Dietrich, and Kenneth L. Shepard*

Cite This: https://doi.org/10.1021/acs.analchem.2c05303 Read Online

ACCESS | Metrics & More | Article Recommendations | Supporting Information

ABSTRACT: Scanning ion conductance microscopy (SICM) is a topographic imaging technique capable of probing biological samples in electrolyte conditions. SICM enhancements have enabled surface charge detection based on voltage-dependent signals. Here, we show how the hopping mode SICM method (HP-SICM) can be used for rapid and minimally invasive surface charge mapping. We validate our method using *Pseudomonas aeruginosa* PA14 (PA) cells and observe a surface charge density of $\sigma_{PA} = -2.0 \pm 0.45$ mC/m^2 that is homogeneous within the ~80 nm lateral scan resolution. This biological surface charge is detected from at least 1.7 μm above the membrane (395× the Debye length), and the long-range charge detection is attributed to electroosmotic amplification. We show that imaging with a nanobubble-plugged probe reduces perturbation of the underlying sample. We extend the technique to PA biofilms and observe a charge density exceeding −20 mC/m^2. We use a solid-state calibration to quantify surface charge density and show that HP-SICM cannot be quantitatively described by a steady-state finite element model. This work contributes to the body of scanning probe methods that can uniquely contribute to microbiology and cellular biology.

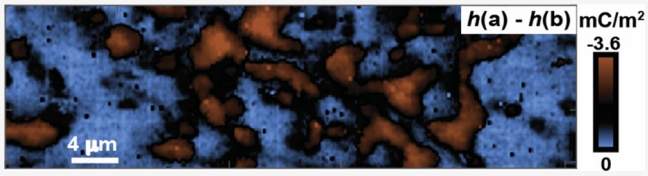

Scanning ion conductance microscopy (SICM) is a topographic imaging technique that maps a surface according to the ion current flow through a scanned probe.[1] SICM enables noncontact imaging in electrolyte solutions with high lateral resolution (<10 nm) roughly equivalent to the diameter of the probe tip.[2] These features make SICM attractive in cellular biology,[3] where it has been applied in bacteria,[4] neurons,[5−9] kidney cells,[10−13] and many other studies.[14−23]

The "hopping mode" SICM (HP-SICM) method was developed to better accommodate soft and heterogeneous biological structures, at the cost of slower imaging.[5] In HP-SICM, the probe records a "baseline current" above each imaging pixel before lowering toward the surface; a relative height is recorded when the baseline current reduces by a predetermined amount (e.g., 1%).

Prior work has augmented SICM beyond topographic mapping,[24−28] including methods that simultaneously record topography and surface charge.[19−23,29−31] These enhancements are notable because surface charge mapping can inform on physiological or chemical functionality, is quantifiable with nanoscale precision using SICM, and is not easily achieved with other tools.

Surface charge detection occurs when the probe signal is influenced by a surface's ionic double layer.[7,21,29,31,32] Under these conditions, the recorded SICM height depends on the probe voltage. Because the voltage mediates the surface interaction, voltage-dependent height recordings in SICM can quantify surface charge.[7,21,31] Prior demonstrations quantify surface charge numerically: a finite element model simulates the probe−surface interaction and uses the surface charge density as a fitting parameter to match experimental data.

Still, challenges remain in SICM-based surface charge detection. The double-layer thickness limits the charge detection range to within 1−2 orders of magnitude beyond the experimental Debye length, which is less than 10 nm for physiological conditions.[7,29,31] It is thus challenging to monitor surface charge and preserve noncontact imaging conditions. Further, the small ratio of double-layer charge to bulk ion concentration results in charge detection methods requiring precisely calibrated systems[21,22] or imaging protocols designed to amplify the probe−surface interaction.[19,20,29,31]

Here, we demonstrate high-speed (>10 pixel/s) and remote (probe tip >395× Debye length away from the surface) surface charge mapping with a hopping mode SICM (HP-SICM) procedure. We validate our technique by imaging single *Pseudomonas aeruginosa* (PA) cells, where we observe the well-characterized negative membrane charge[33−35] from at least 395× the experimental Debye length. The long-range capability is enabled by rapid probe approach speeds (2−20 μm/s) that also enable scan rates as fast as 14 pixel/s. We use a solid-state

Received: November 28, 2022
Accepted: March 1, 2023

calibration procedure to quantify the membrane charge as $\sigma_{PA} = -2.0 \pm 0.45$ mC/m^2. This charge appears homogeneous at the ∼80 nm lateral scan resolution. We show how a nanobubble-filled HP-SICM probe enables weakly adhered single PA cells to be imaged without desorption. We extend HP-SICM to imaging of PA Δ*phz* colony biofilms, i.e., biofilms that are incapable of producing charged phenazines (a cellular metabolite used as an electron shuttle).[30,36] We capture the biofilm topography in situ with nanoscale resolution and show that it possesses a negative charge exceeding −20 mC/m^2. Our HP-SICM method achieves minimally invasive surface charge mapping at >10 pixel/s and is readily implemented with standard SICM equipment.

■ EXPERIMENTAL SECTION

Scanning Ion Conductance Microscopy. We use the NX-Bio (Park Systems) tool with an AxoPatch 200B (Molecular Devices) current amplifier. Currents are sampled at 10 kHz and processed in XEP (Park) and Clampex (MD) software. HP-SICM is conducted with a 1 μm retract height, 1% threshold current ($I^* = 0.99I_{lim}$), and 2−20 μm/s approach speed. Topographic data are processed using XEI (Park) and MATLAB software.

Pseudomonas aeruginosa. For single-cell experiments, PA14 (UCBPP-PA14)[37] wild-type cells are used. For colony biofilm experiments, wild-type PA14 or PA14 Δ*phz* mutant[38] cells are used. More details are included in the Supporting Information (Note S1).

Substrate Preparation. A polystyrene dish is used with a Cell-Tak (Corning) coating to immobilize cells. More details are included in the Supporting Information (Note S2).

Probe Fabrication and Electrolyte Composition. Nanopipette probes are pulled from 1.0/0.5 mm boroscilicate capillaries with a P-97 (Sutter): $P = 500|H = 590|Vel = 0|Pul = 25|Del = 80$. Tip diameters (65−250 nm) are determined by the capillary thickness and deduced from ion current data. Smaller probes improve lateral resolution at the cost of SNR. KCl electrolyte solutions are adjusted to pH 7 with KOH.

Solid-State Surface Charge Calibration. Varying surface potentials are applied to solid-state electrodes to modulate the surface charge. The HP-SICM step height at the electrode edge is recorded for varying surface and probe potentials. More details are included in the Supporting Information (Note S3).

Finite-Element Modeling. COMSOL v5.4 is used to numerically simulate HP-SICM experiments. More details are included in the Supporting Information (Note S4).

Dynamic Light Scattering. The zeta potential for PA cells is determined by dynamic light scattering (DLS) measured by a Zetaszier (Malvern).

■ RESULTS AND DISCUSSION

Topographic SICM Verification. We verify topographic data from HP-SICM by scanning individual PA cells.[39] The nanopipette probe scans over a PA cell-coated substrate with a voltage difference (V) driving an ionic current (I) between a working Ag/AgCl electrode inside the probe and a grounded Ag/AgCl reference electrode in the electrolyte. In the hopping mode, the probe records a baseline current over the substrate (I_{lim}), lowers toward the substrate, and registers a relative pixel height when the current reduces to the predetermined threshold value ($I^* = 0.99I_{lim}$). The probe then retracts and repeats the approach procedure.

PA cells weakly adhere to substrates and are susceptible to desorption.[40,41] Low electrolyte concentrations (≤5 mM) are required for electrostatic adhesion. Desorption is mitigated when less fluid flows through the probe, e.g., due to a smaller-diameter probe or a nanobubble-plugged probe. Immobilization also requires a substrate coated with tacky protein and treated with a deposition/washing procedure (Note S2 and Figures S1, S2). Without washing, floating cells can spontaneously order into film-like structures (Figure S3). This process may promote biofilm nucleation[42] and is observed to increase desorption.

Imaging is verified by comparing an HP-SICM micrograph (Figure 1a) to optically visible cell morphologies (Figure S4).

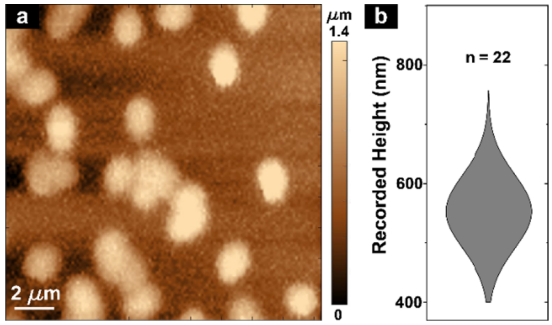

Figure 1. (a) HP-SICM micrograph of PA cells on a polystyrene surface. (b) Height distribution for the cells depicted in (a).

The PA cells are recorded as hemispheroid protrusions with a Gaussian height distribution between 400 and 750 nm (Figure 1b). Experimental conditions are $V = 200$ mV and a ∼100 nm diameter probe. Round PA cells are observed in contrast to the typical rod-shaped geometry,[43] which is attributed to a biological response to the nutrient-deficient electrolyte. Additional micrographs illustrate the rest of the experimental verification (Figure S5).

Surface Charge Detection with HP-SICM. Voltage-dependent and surface charge-mediated HP-SICM data are demonstrated over a single immobilized PA cell. Consecutive line scans with varying probe voltages record drastically different topographies (Figure 2a). Imaging is done with $V = \pm 200$ and ±150 mV, a ∼150 nm diameter probe, and a 6 μm/s approach speed. Reported heights depict mean values (with standard deviations) across three scans. The positive-voltage scans capture overlapping profiles with height $H_{PA} = 497$ nm. In contrast, the negative-voltage scans capture a pit with a voltage-dependent depth.

Comparing the $V = \pm 200$ mV data, a height discrepancy $\Delta h = 732$ nm is observed. This Δh represents the minimum value for the probe-surface separation distance at which I^* is recorded, based on the cell not being contacted during imaging. Because the membrane charge is first detected at the edge of the cell, the data indicate that the charge detection range is at least 170× the experimental Debye length ($\kappa^{-1} = 4.3$ nm).

Thus, Figure 2a contains a pair of true topographies and a pair of charge-mediated topographies. The agreement between the positive voltage data shows that probe−surface interactions are negligible in this configuration, making these data control measures. The negative voltage data show that surface charge interactions can significantly modulate the HP-SICM signal. Smooth topographies recorded with negative voltages suggest that this surface charge is uniformly distributed with respect to the lateral resolution of these scans (∼80 nm).

https://doi.org/10.1021/acs.analchem.2c05303
Anal. Chem. XXXX, XXX, XXX−XXX

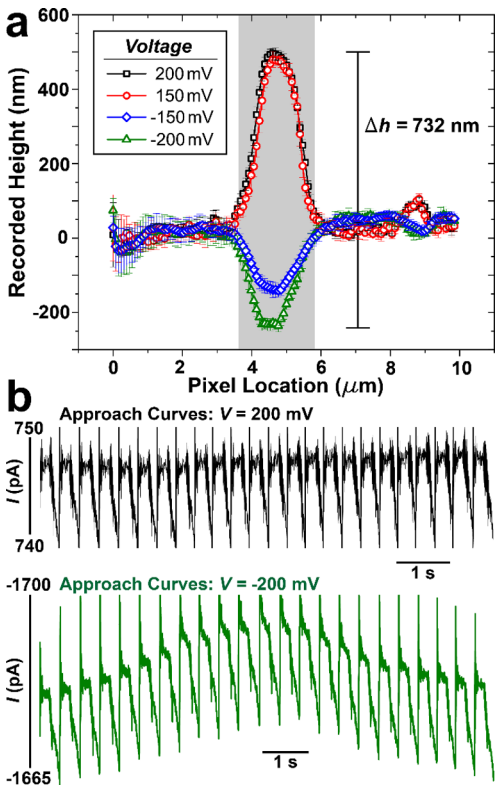

Figure 2. (a) Voltage-dependent HP-SICM topographies consecutively recorded over a single PA cell. (b) Ion current approach curves for the shaded pixels in (a). The data show voltage-dependent and charge-mediated HP-SICM signals.

DLS supports the data as being attributable to the PA cell's negative membrane charge.[33] DLS indicates a surface charge density $\sigma_{PA} = -3.3$ mC/m^2 for suspended PA cells (Figure S6), consistent with prior reports.[34,35,44]

Voltage-dependent I_{lim} increases over the PA membrane (Figure 2b) further attest to the charge detection capabilities of HP-SICM. Approach curves over the cell (shaded region in Figure 2a) show consistent I_{lim} values at V = 200 mV and amplified I_{lim} values at $V = -200$ mV. Amplified I_{lim} values arise due to the transfer of charged fluid from the membrane surface into the probe tip. I_{lim} increases the scale with the membrane height and similarly occurs at $V = -150$ mV (Figure S7).

Electrokinetic Model for Charge Detection with HP-SICM. Having demonstrated voltage-dependent and surface-charge-mediated HP-SICM data, we describe the relevant physical mechanism. When approaching a negatively charged surface with a negative probe voltage, the double-layer fluid enters the probe tip to add conductance and oppose the proximity-based impedance increase. As a result, I^* is recorded nearer to the surface than in the absence of charge. Approaching the same surface with a positive probe voltage, the repulsive effect is negligible.

Therefore, HP-SICM data recorded with equal and opposite probe voltages yield a set of control pixels (equivalent voltage and charge polarity) and a set of charge-detecting pixels (opposing polarities). A schematic depicts these dynamics over a PA cell (Figure 3), which presents a negative membrane charge due to lipopolysaccharides (LPS).[33]

We attribute the strong surface effect ($\Delta h > H_{PA}$) and long detection range ($170\kappa^{-1}$) to fluid flows driven by electroosmosis and the approaching probe velocity (2−20 μm/s).[45,46]

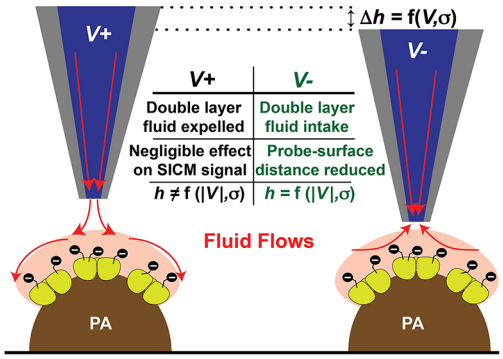

Figure 3. Electrokinetic mechanism for PA cell membrane charge detection using HP-SICM.

These flows amplify the probe-surface interaction by enriching the inner probe tip with charged fluid. They also extend the probe-surface separation to more than 3.5× greater than the distances predicted by an electrophoretic transport model (∼200 nm).[47,48] Based on I_{lim} increases that are measured when the probe is stationary, the charged fluid remains in the probe and thus adds current to the I_{lim} signal.

Calibrating HP-SICM with a Solid-State Surface To Quantify Surface Charge Density. We scan an electrode-SU8 interface to quantify voltage-dependent height discrepancies as functions of charge density (Note S3). We then derive a transfer function that relates the HP-SICM height to the underlying surface charge, e.g., $\sigma_{PA} = f(\Delta h)$.

The solid-state model reproduces the trends observed over the biological sample. With the probe voltage $V = -200$ mV, the recorded interface height increases with increasing magnitude of negative surface charge (Figure 4a), as the probe lowers closer to

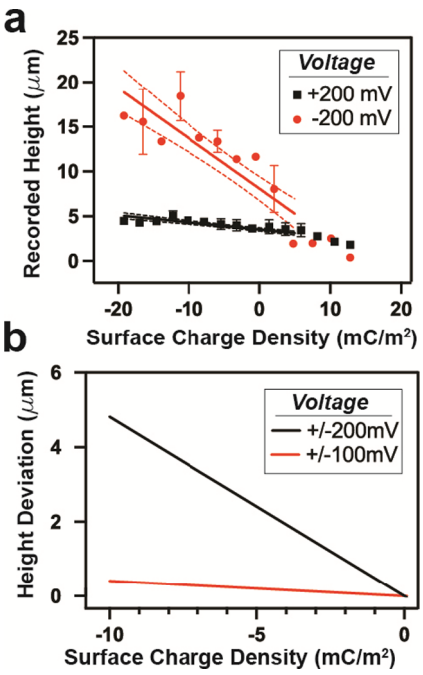

Figure 4. (a) HP-SICM heights recorded over a SU-8-platinum surface electrode interface while sweeping the charge on the platinum surface. (b) Transfer functions for relating HP-SICM height deviations to underlying charge densities, based on fitting of the data in (a) and Figure S8.

https://doi.org/10.1021/acs.analchem.2c05303
Anal. Chem. XXXX, XXX, XXX−XXX

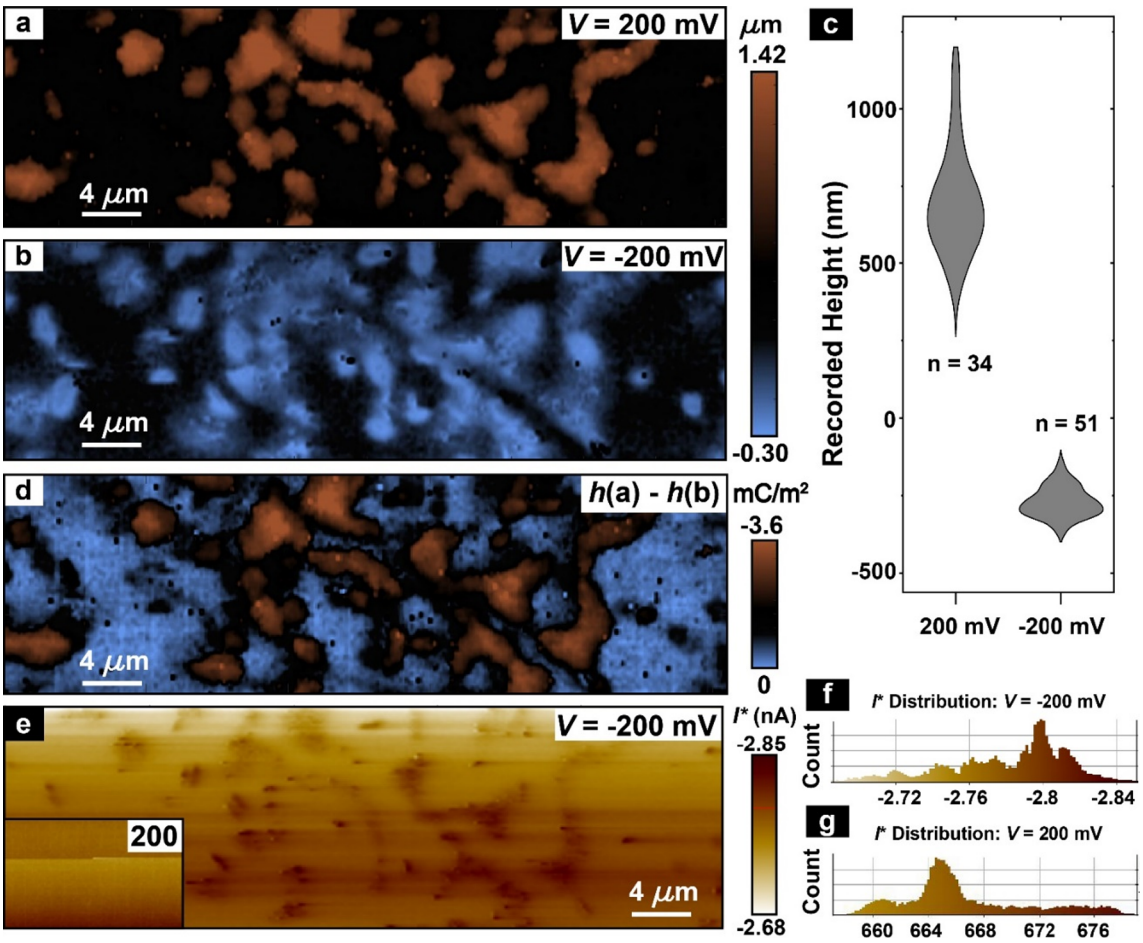

Figure 5. (a, b) Consecutive HP-SICM micrographs with probe voltages $V = \pm 200$ mV, plotted on a bipolar color scale. (c) Voltage-dependent PA cell heights recorded in micrographs (a, b). (d) Quantitative surface charge mapping, based on the height deviations between (a, b) and the $\lambda_{200} = 0.48$ μm/[mC/m^2] calibration factor derived in Figure 4. (e) Threshold currents (I^*) corresponding to the micrograph pixels in (b) and (inset) (a). (f, g) I^* distributions for the micrographs in (e).

the negatively charged electrode before recording I^*. With the probe voltage at $V = 200$ mV, the recorded interface height is minimally affected by the negative surface charge. Upon repeating the solid-state calibration experiments with $V = \pm 100$ mV, similar trends are observed with reduced sensitivity (Figure S8).

Surprisingly, the calibration reveals our HP-SICM configuration to be insensitive to positive surface charge (Figure 4a). We attribute this to the intrinsic negative charge on the glass probe, which rejects double-layer fluid intake over positively charged surfaces and inhibits the probe-surface interaction. Thus, a probe modified to be positively charged (e.g., by coating with PLL) or uncharged (e.g., by metallization) is needed for positive or bipolar charge detection, respectively.

We derive transfer functions that relate height deviations to negative surface charge densities. This is done by fitting trend lines to the solid-state interface heights recorded at $V = \pm 200$ and ± 100 mV (Figures 4a and S8). For each voltage pair, the transfer function is calculated as the difference between the two trend line slopes. With $V = \pm 200$ mV, we observe charge sensitivity $\lambda_{200} = 0.48$ μm/[mC/m^2]; with $V = \pm 100$ mV, $\lambda_{100} = 0.041$ μm/[mC/m^2] (Figure 4b). For a pair of HP-SICM heights recorded with equal and opposite voltages, the charge density can thus be determined as $\sigma = \Delta h/\lambda$.

The quantification procedure is verified by comparing the σ_{PA} values predicted by HP-SICM to that measured by DLS (-3.3 mC/m^2). Excellent agreement is observed, with the range of height deviations across all ± 200 mV experiments ($\Delta h = 0.73-1.7$ μm) placing σ_{PA} in the range of -1.5 to -3.6 mC/m^2.

Large-Area Charge Mapping with HP-SICM. With our calibrated HP-SICM system, we perform charge mapping. Consecutive scans recorded with a ~250 nm-diameter probe show many protruding cells with $V = 200$ mV that appear as pits with $V = -200$ mV (Figure 5a,b). With $V = 200$ mV, average heights are $H_{PA} = 701 \pm 167$ nm; with $V = -200$ mV, average heights are $H_{PA} = -271 \pm 48$ nm (Figure 5c). Because these cells did not desorb after two scans, we consider the procedure to be noncontact and noninvasive. We attribute oblong, crescent, and other irregular cell shapes to clusters where individual cells are separated by distances less than the lateral scan resolution. The average charge is thus $\sigma_{PA} = -2.0 \pm 0.45$ mC/m^2. The dynamic range $\Delta h = 1.7$ μm indicates that in this experiment, surface charge detection is achieved at distances of more than 395× the Debye length. More cells are reported with $V = -200$ mV because this scan was executed first. Discrepancies across the image pair are attributed to surface adsorption/desorption or flagellar rotation.[49]

We generate a surface charge map (Figure 5d) by first plotting the pixel-level height deviations between the $V = \pm 200$ mV scans

https://doi.org/10.1021/acs.analchem.2c05303
Anal. Chem. XXXX, XXX, XXX−XXX

and then scaling the resulting heights by the coefficient (λ_{200}) of the transfer function described above. The charge map shows negative charge density over all PA cells and negligible charge density over the polystyrene substrate.

When using a probe of this diameter, cells do not desorb due to the presence of a nanobubble in the tip. We previously showed that electrolyte-filled nanopipette tips may contain metastable nanobubbles, as evidenced by enhanced current rectification, reduced conductance, and increased noise when compared to nanobubble-free channels.[50] When the volume of such a nanobubble is small compared to the volume of the tip, these aforementioned effects are minimal and slowly become more pronounced as the nanobubble grows over several hours. During SICM scans, gradual decreases in conductance (e.g., Figures 5e and S9) are therefore attributed to slowly growing nanobubbles. Remarkably, in these experiments, the presence of a small nanobubble is beneficial (despite the slightly reduced SNR) because of the nanobubble's fluid-blocking effect and the resulting ability to less invasively image the PA cells.

The I^* signals (Figure 5e) confirm that these experiments occur under the presence of nanobubbles. We note that $|I^*|$ is directly measured during HP-SICM and serves as a proxy measure for I_{lim} and conductance shifts. In addition to I_{lim} shifts observed over cells, we observe I_{lim} decreases across the bottom-to-top scan direction (Figure 5e and inset). These I_{lim} decreases confirm the presence of a slowly growing nanobubble inside the probe and are replicated in a different experiment (Figure S9). Similarly supporting these claims are enhanced current rectification (~4.2×) and aggregate I^* counts showing Gaussian distributions with drifts (and secondary peaks when $V = -200$ mV) (Figures 5f,g and S9). We note that across more than $n = 100$ attempts to scan PA cells without a nanobubble in the probe, cells consistently desorb after multiple scans.

Finite-Element Modeling of the HP-SICM System. We explore whether a finite-element model (FEM) can describe HP-SICM and obviate the need for solid-state calibrations.[29,32] To enable this, a new experiment is performed with a nanobubble-free probe to simplify the fluid dynamics. Without the nanobubble's fluid blocking, a smaller ~65 nm-diameter probe is required to keep cells immobilized. The proximal area scans are plotted with the heights normalized against the flat substrate (Figure 6a,b). An adequate quantity of cells is captured to permit FEM characterization. However, these cells are perturbed during scanning, as evidenced by geometric distortions.

The FEM simulates approach curves under varying probe voltages and surface charges (Note S4 and Figure S10). Simulated I/I_{lim} values fit to experimental values (Figure 6c, table).

The FEM cannot quantitatively reproduce HP-SICM data due to the invalidity of the steady-state assumption. This is consistent with the experimental I_{lim} shifts due to the transient accumulation of charged fluid. Due to imposing steady-state transport, the FEM simulates the approach current to reduce to I^* only after the probe is within 100 nm of the surface (Figure S10), which is at least 7−10× closer than in experiments. An accurate FEM would require a transient solver and time-modulating geometry.

A comparison of normalized currents recorded and simulated over the highlighted pixels of Figure 6a,b (Δ, *) shows the quantitative limits of the FEM (Figure 6c, solid lines). To fit the simulated $I > I_{lim}$ peak to the experimental data,[18] a simulated current density of $\sigma_{PA} = -30$ mC/m^2 is required. Even so, the

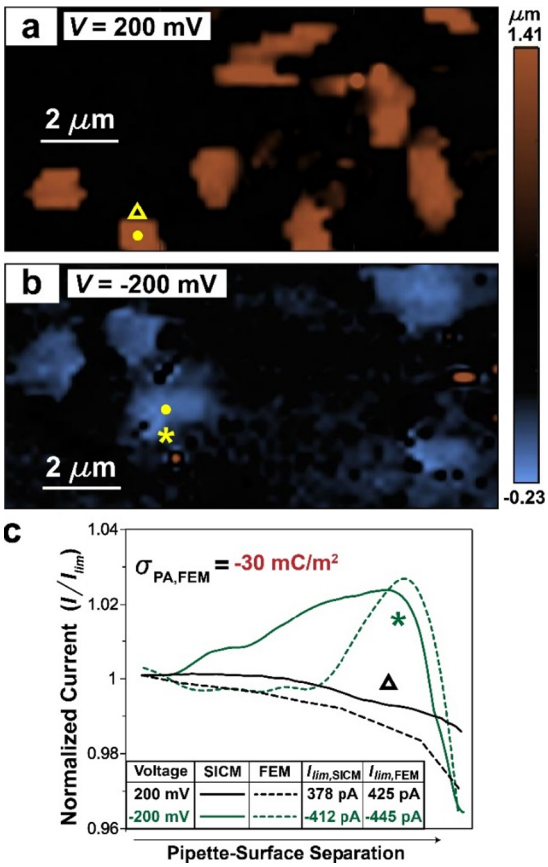

Figure 6. (a, b) HP-SICM micrographs recorded over proximal areas of a substrate, plotted on a bipolar color scale. (c) Experimental approach curves recorded at the highlighted pixels in (a, b) (solid lines) are overlaid with simulated approach curves using a finite element model (dashed lines). Quantitative inaccuracy of FEM, due to the invalidity of the steady-state assumption, is reflected by the simulated surface charge being 10× greater than the true value.

qualitative accuracy of the FEM is further supported by the simulated peak only occurring in the approach velocity range of 15−40 μm/s (Figure S11), consistent with experimental velocities (Figure S12).

PA Biofilm Imaging. In nature, PA exists in biofilms where many cells co-exist in a self-produced, hydrated polysaccharide matrix.[33] Better understanding of biofilms has relevance to public health and biofouling mitigation. The topographic charge distribution of the matrix material and how matrix structures support biofilm physiology are unknown. To our knowledge, biofilm matrix topography has yet to be measured in situ with nanoscale resolution.

We thus image the in situ topography of PA Δ*phz* biofilm cross-sections (Figure S13). The Δ*phz* mutant is studied because of increased matrix production compared to wild-type biofilms.[51] The increased porosity of the wild-type matrix limits its hindrance of ion flow, such that the approaching probe does not record an I^* signal.

A large-area micrograph depicts the biofilm's polysaccharide matrix (Figure 7a). An amorphous mesh with a large distribution of pore sizes between 500 nm and 3 μm is observed. The image is recorded at $V = 200$ mV with a ~40 nm diameter probe and a 30 mM electrolyte. Because the biofilm easily adheres to the surface, we can use a more concentrated electrolyte to enable a smaller probe and improved lateral resolution.

https://doi.org/10.1021/acs.analchem.2c05303
Anal. Chem. XXXX, XXX, XXX−XXX

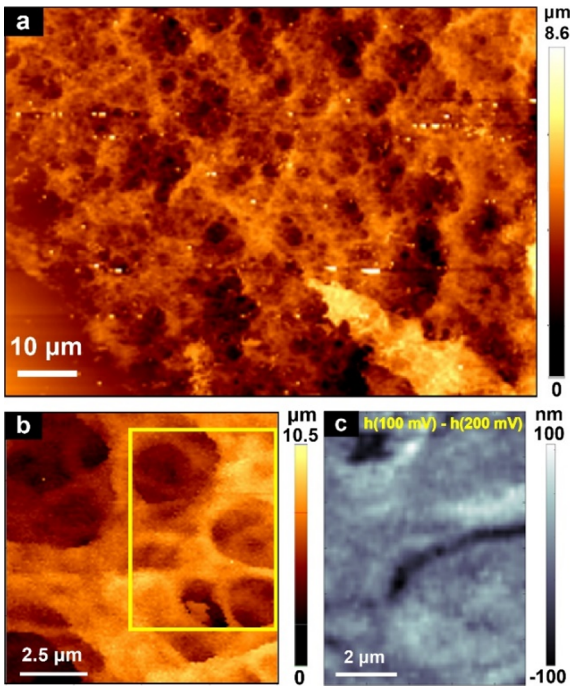

Figure 7. (a, b) HP-SICM micrographs of PA Δ*phz* biofilms recorded with V = 200 mV. (c) Difference map of the highlighted region in (b) subtracted from a subsequent micrograph taken with V = 100 mV.

We attempt to replicate the initial scan with a negative voltage and map the biofilm's surface charge distribution. However, the biofilm charge causes the probe current to increase through the approach, and I^* is never recorded (Figure S14). This dynamic cannot be overcome by modifying the probe size, approach speed, or electrolyte concentration. Thus, the biofilm presents a surface charge exceeding the −20 mC/m^2 limit investigated over the solid-state reference electrode.

For completeness, we compare biofilm scans across two positive voltages. These images are captured by scanning with V = 200 mV (Figure 7b) and then with V = 100 mV (Figure S15). A topographic difference map is generated by subtracting the V = 200 mV signal from the V = 100 mV signal (Figure 7c). The small dynamic range of the difference map (200 nm, versus 10.5 μm in the source images) indicates that neither of these datasets is strongly influenced by the biofilm charge. This is consistent with the probe's insensitivity to both positive charge detection and the repulsive probe−surface interaction.

CONCLUSIONS

In this work, we demonstrate how hopping mode SICM (HP-SICM) can be used for nanoscale surface charge detection by imaging PA cells. Voltage-dependent HP-SICM heights recorded over PA cells are translated into surface charge densities using a solid-state calibration. With this calibration, HP-SICM estimates the PA cell membrane charge to be σ_{PA} = −2.0 ± 0.45 mC/m^2, in agreement with DLS data. Smooth membrane surfaces (recorded under charge-detecting conditions) indicate the PA membrane charge to be homogeneously distributed at the lateral scan resolution (∼80 nm). We show that during HP-SICM, surface charge influences topographic measurements through attractive interactions between the probe and the ionic double layer. Due to amplification from fluid outflows and electroosmosis, the probe detects the PA membrane charge from as far as 395× the Debye length.

The data provide insights into PA cells, PA14 Δ*phz* biofilms, and investigating these samples with SICM. Because single cells adhere weakly to substrates, we show that a nanobubble-filled SICM probe reduces fluid outflows to permit less invasive imaging. We image Δ*phz* biofilms in situ and show the biofilm matrix to possess a net negative charge exceeding −20 mC/m^2.

Our HP-SICM charge detection method builds upon emerging capabilities in microbiology. It enables nanoscale charge mapping, promotes noncontact imaging, is robust to biological specimens, supports scan rates in excess of 10 pixels/s, and can be performed with standard SICM tools. With a positively charged probe, future scans of PA biofilms might find positively charged subdomains[52] within the (overall negatively charged) biofilm matrix. Such insight into PA charge distribution may inform on antibacterial coatings[53−55] or cell-surface adhesion properties.[43,56,57] With multifunctional scanning probes,[58] surface charge detection could be done in parallel with other methods for studying the antibiotic response[59] and biofilm nucleation[42] of PA and other microbes.

ASSOCIATED CONTENT

Supporting Information

The Supporting Information is available free of charge at https://pubs.acs.org/doi/10.1021/acs.analchem.2c05303.

Preparation of *Pseudomonas aeruginosa*; PA cell immobilization and substrate preparation; electrode fabrication and experimentation; finite element procedure and limitations; procedural effects on morphology and substrate affinity for deposited PA cells; SICM-induced desorption of immobilized cells; floating film-like PA structures; optical micrograph of the HP-SICM experiment; representative topographic SICM images; zeta potential measurement and surface charge calculation for PA cells; voltage-dependent and surface charge-mediated baseline current shifts in Figure 2; surface charge detection over the solid-state interface with V = ±100 mV; repeated non-contact imaging with a nanobubble-plugged nanopipette; finite element model for simulating SICM recording; influence of surface charge and approach speed on simulated approach curves; repeated current peaking and FEM-based charge fitting for the data in Figure 6; overview of biofilm experiments; charge-saturated approach curves when scanning biofilms with negative voltages; and V = 100 mV micrograph for generating the difference map in Figure 7 (PDF)

AUTHOR INFORMATION

Corresponding Author

Kenneth L. Shepard − *Department of Electrical Engineering, Columbia University, New York, New York 10027, United States*; orcid.org/0000-0003-0665-6775; Email: shepard@ee.columbia.edu

Authors

Jake Rabinowitz − *Department of Electrical Engineering, Columbia University, New York, New York 10027, United States*

Andreas J. W. Hartel − *Department of Electrical Engineering and Department of Biology, Columbia University, New York, New York 10027, United States*; orcid.org/0000-0002-2693-4472

https://doi.org/10.1021/acs.analchem.2c05303
Anal. Chem. XXXX, XXX, XXX−XXX

Hannah Dayton − *Department of Biology, Columbia University, New York, New York 10027, United States*
Jason D. Fabbri − *Department of Electrical Engineering, Columbia University, New York, New York 10027, United States*; orcid.org/0000-0001-5459-4199
Jeanyoung Jo − *Department of Biology, Columbia University, New York, New York 10027, United States*
Lars E. P. Dietrich − *Department of Biology, Columbia University, New York, New York 10027, United States*

Complete contact information is available at:
https://pubs.acs.org/10.1021/acs.analchem.2c05303

Author Contributions

[§]J.R. and A.J.W.H. contributed equally. J.R. and A.J.W.H. conducted the SICM experiments. J.R., A.J.W.H., H.D., and J.J. prepared biological samples. J.R., A.J.W.H., J.F., and J.J. prepared samples for imaging. J.R., A.J.W.H., L.E.P.D, and K.L.S. analyzed the results. K.L.S. provided overall project support and supervision. J.R. wrote the manuscript. All authors edited and commented on the manuscript.

Notes

The authors declare no competing financial interest.

■ ACKNOWLEDGMENTS

This work was supported in part by the National Science Foundation under Grant 1353553 to K.L.S. and National Institute of Health under Grant R01AI103369 to L.E.P.D. We acknowledge Alexa Price-Whelan for reviewing the manuscript.

■ REFERENCES

(1) Hansma, P. K.; Drake, B.; Marti, O.; Gould, S. A. C.; Prater, C. B. *Science* **1989**, *243*, 4891.
(2) Shevchuk, A. I.; Frolenkov, G. I.; Sánchez, D.; James, P. S.; Freedman, N.; Lab, M. J.; Jones, R.; Klenerman, D.; Korchev, Y. E. *Angew. Chem., Int. Ed.* **2006**, *45*, 2212−2216.
(3) Leitao, S. M.; Drake, B.; Pinjusic, K.; Pierrat, X.; Navikas, V.; Nievergelt, A. P.; Brillard, C.; Djekic, D.; Radenovic, A.; Persat, A.; Constam, D. B.; Anders, J.; Fantner, G. E. *ACS Nano* **2021**, *15*, 17613−17622.
(4) Cremin, K.; Jones, B. A.; Teahan, J.; Meloni, G. N.; Perry, D.; Zerfass, C.; Asally, M.; Soyer, O. S.; Unwin, P. R. *Anal. Chem.* **2020**, *92*, 16024−16032.
(5) Novak, P.; Li, C.; Shevchuk, A. I.; Stepanyan, R.; Caldwell, M.; Hughes, S.; Smart, T. G.; Gorelik, J.; Ostanin, V. P.; Lab, M. J.; Moss, G. W. J.; Frolenkov, G. I.; Klenerman, D.; Korchev, Y. E. *Nat. Methods* **2009**, *6*, 279−281.
(6) Takahashi, Y.; Shevchuk, A. I.; Novak, P.; Babakinejad, B.; Macpherson, J.; Unwin, P. R.; Shiku, H.; Gorelik, J.; Klenerman, D.; Korchev, Y. E.; Matsue, T. *Proc. Natl. Acad. Sci. U. S. A.* **2012**, *109*, 11540−11545.
(7) Clarke, R. W.; Zhukov, A.; Richards, O.; Johnson, N.; Ostanin, V.; Klenerman, D. *J. Am. Chem. Soc.* **2013**, *135*, 322−329.
(8) Takahashi, Y.; Ito, K.; Wang, X.; Matsumae, Y.; Komaki, H.; Kumatani, A.; Ino, K.; Shiku, H.; Matsue, T. *Electrochemistry* **2014**, *82*, 331−334.
(9) Takahashi, Y.; Zhou, Y.; Miyamoto, T.; Higashi, H.; Nakamichi, N.; Takeda, Y.; Kato, Y.; Korchev, Y.; Fukuma, T. *Anal. Chem.* **2020**, *92*, 2159−2167.
(10) Zhou, L.; Gong, Y. V.; Hou, J.; Baker, L. A. *Anal. Chem.* **2017**, *89*, 13603−13609.
(11) Zhou, L.; Gong, Y.; Sunq, A.; Hou, J.; Baker, L. A. *Anal. Chem.* **2016**, *88*, 9630−9637.
(12) Simeonov, S.; Schäffer, T. E. *Nanoscale* **2019**, *11*, 8579−8587.
(13) Navikas, V.; Leitao, S. M.; Grussmayer, K. S.; Descloux, A.; Drake, B.; Yserentant, K.; Werther, P.; Herten, D. P.; Wombacher, R.; Radenovic, A.; Fantner, G. E. *Nat. Commun.* **2021**, *12*, 4565.
(14) Korchev, Y. E.; Gorelik, J.; Lab, M. J.; Sviderskaya, E. V.; Johnston, C. L.; Coombes, C. R.; Vodyanoy, I.; Edwards, C. R. W. *Biophys. J.* **2000**, *78*, 451−457.
(15) Ushiki, T.; Nakajima, M.; Choi, M. H.; Cho, S. J.; Iwata, F. *Micron* **2012**, *43*, 1390−1398.
(16) Zhang, S.; Cho, S. J.; Busuttil, K.; Wang, C.; Besenbacher, F.; Dong, M. *Nanoscale* **2012**, *4*, 3105−3110.
(17) Rheinlaender, J.; Geisse, N. A.; Proksch, R.; Schäffer, T. E. *Langmuir* **2011**, *27*, 697−704.
(18) Ushik, T.; Ishizaki, K.; Mizutani, Y.; Nakajima, M.; Iwata, F. *Chromosome Res.* **2021**, *29*, 95−106.
(19) Perry, D.; Paulose Nadappuram, B.; Momotenko, D.; Voyias, P. D.; Page, A.; Tripathi, G.; Frenguelli, B. G.; Unwin, P. R. *J. Am. Chem. Soc.* **2016**, *138*, 3152−3160.
(20) Page, A.; Perry, D.; Young, P.; Mitchell, D.; Frenguelli, B. G.; Unwin, P. R. *Anal. Chem.* **2016**, *88*, 10854−10859.
(21) Klausen, L. H.; Fuhs, T.; Dong, M. *Nat. Commun.* **2016**, *7*, 12447.
(22) Fuhs, T.; Klausen, L. H.; Sønderskov, S. M.; Han, X.; Dong, M. *Nanoscale* **2018**, *10*, 4538−4544.
(23) Page, A.; Kang, M.; Armitstead, A.; Perry, D.; Unwin, P. R. *Anal. Chem.* **2017**, *89*, 3021−3028.
(24) Ying, L.; Bruckbauer, A.; Zhou, D.; Gorelik, J.; Shevchuk, A.; Lab, M.; Korchev, Y.; Klenerman, D. *Phys. Chem. Chem. Phys.* **2005**, *7*, 2859−2866.
(25) Chen, C. C.; Zhou, Y.; Baker, L. A. *Annu. Rev. Anal. Chem.* **2012**, *5*, 207−228.
(26) Page, A.; Perry, D.; Unwin, P. R. *Proc. R. Soc. A* **2017**, *473*, 20160889.
(27) Ma, Y.; Wang, D. *Anal. Chem.* **2021**, *93*, 15821−15825.
(28) Zhu, C.; Jagdale, G.; Gandolfo, A.; Alanis, K.; Abney, R.; Zhou, L.; Bish, D.; Raff, J. D.; Baker, L. A. *Environ. Sci. Technol.* **2021**, *55*, 12233−12242.
(29) McKelvey, K.; Kinnear, S. L.; Perry, D.; Momotenko, D.; Unwin, P. R. *J. Am. Chem. Soc.* **2014**, *136*, 13735−13744.
(30) Perry, D.; Al Botros, R.; Momotenko, D.; Kinnear, S. L.; Unwin, P. R. *ACS Nano* **2015**, *9*, 7266−7276.
(31) Zhu, C.; Zhou, L.; Choi, M.; Baker, L. A. *ChemElectroChem* **2018**, *5*, 2986−2990.
(32) Sa, N.; Lan, W. J.; Shi, W.; Baker, L. A. *ACS Nano* **2013**, *7*, 11272−11282.
(33) Hobot, J. A. Bacterial Ultrastructure. In *Molecular Medical Microbiology: Second Edition*; 2015; vol *1*−*3*, pp 7−32.
(34) Bruinsma, G. M.; Rustema-Abbing, M.; Van Der Mei, H. C.; Busscher, H. J. *J. Microbiol. Methods* **2001**, *45*, 95−101.
(35) Soni, K. A.; Balasubramanian, A. K.; Beskok, A.; Pillai, S. D. *Curr. Microbiol.* **2008**, *56*, 93−97.
(36) Price-Whelan, A.; Dietrich, L. E. P.; Newman, D. K. *Nat. Chem. Biol.* **2006**, *2*, 71−78.
(37) Lee, D. G.; Urbach, J. M.; Wu, G.; Liberati, N. T.; Feinbaum, R. L.; Miyata, S.; Diggins, L. T.; He, J.; Saucier, M.; Déziel, E.; Friedman, L.; Li, L.; Grills, G.; Montgomery, K.; Kucherlapati, R.; Rahme, L. G.; Ausubel, F. M. *Genome Biol.* **2006**, *7*, R90.
(38) Dietrich, L. E. P.; Price-Whelan, A.; Petersen, A.; Whiteley, M.; Newman, D. K. *Mol. Microbiol.* **2006**, *61*, 1308−1321.
(39) Liberati, N. T.; Urbach, J. M.; Miyata, S.; Lee, D. G.; Drenkard, E.; Wu, G.; Villanueva, J.; Wei, T.; Ausubel, F. M. *Proc. Natl. Acad. Sci. U. S. A.* **2006**, *103*, 2833−2838.
(40) Louise Meyer, R.; Zhou, X.; Tang, L.; Arpanaei, A.; Kingshott, P.; Besenbacher, F. *Ultramicroscopy* **2010**, *110*, 1349−1357.
(41) Doktycz, M. J.; Sullivan, C. J.; Hoyt, P. R.; Pelletier, D. A.; Wu, S.; Allison, D. P. *Ultramicroscopy* **2003**, *97*, 209−216.
(42) Connell, J. L.; Kim, J.; Shear, J. B.; Bard, A. J.; Whiteley, M. *Proc. Natl. Acad. Sci. U. S. A.* **2014**, *111*, 18255−18260.
(43) Mitik-Dineva, N.; Wang, J.; Truong, V. K.; Stoddart, P.; Malherbe, F.; Crawford, R. J.; Ivanova, E. P. *Curr. Microbiol.* **2009**, *58*, 268−273.

(44) Bard, A. J.; Faulkner, L. R. *Fundamentals and Applications*; 1980.
(45) Rabinowitz, J.; Edwards, M. A.; Whittier, E.; Jayant, K.; Shepard, K. L. *J. Phys. Chem. A* **2019**, *123*, 8285−8293.
(46) Teahan, J.; Perry, D.; Chen, B.; McPherson, I. J.; Meloni, G. N.; Unwin, P. R. *Anal. Chem.* **2021**, *93*, 12281−12288.
(47) Rheinlaender, J.; Schäffer, T. E. *Anal. Chem.* **2017**, *89*, 11875−11880.
(48) Sa, N.; Baker, L. A. *J. Am. Chem. Soc.* **2011**, *133*, 10398−10401.
(49) Qian, C.; Ching Wong, C.; Swarup, S.; Chiama, K. H. *Appl. Environ. Microbiol.* **2013**, *79*, 4734−4743.
(50) Rabinowitz, J.; Whittier, E.; Liu, Z.; Jayant, K.; Frank, J.; Shepard, K. *Sci. Adv.* **2020**, *6*, No. eabd0126.
(51) Okegbe, C.; Fields, B. L.; Cole, S. J.; Beierschmitt, C.; Morgan, C. J.; Price-Whelan, A.; Stewart, R. C.; Lee, V. T.; Dietrich, L. E. P. *Proc. Natl. Acad. Sci. U. S. A.* **2017**, *114*, E5236−E5245.
(52) Jennings, L. K.; Storek, K. M.; Ledvina, H. E.; Coulon, C.; Marmont, L. S.; Sadovskaya, I.; Secor, P. R.; Tseng, B. S.; Scian, M.; Filloux, A.; Wozniak, D. J.; Howell, P. L.; Parsek, M. R. *Proc. Natl. Acad. Sci. U. S. A.* **2015**, *112*, 11353−11358.
(53) Pasmore, M.; Todd, P.; Pfiefer, B.; Rhodes, M.; Bowman, C. N. *Biofouling* **2002**, *18*, 65−71.
(54) Rzhepishevska, O.; Hakobyan, S.; Ruhal, R.; Gautrot, J.; Barbero, D.; Ramstedt, M. *Biomater. Sci.* **2013**, *1*, 589−602.
(55) Kao, W. K.; Gagnon, P. M.; Vogel, J. P.; Chole, R. A. *Laryngoscope* **2017**, *127*, 1655−1661.
(56) Poortinga, A. T.; Bos, R.; Norde, W.; Busscher, H. J. *Surf. Sci. Rep.* **2002**, *47*, 1−32.
(57) Hsu, L. C.; Fang, J.; Borca-Tasciuc, D. A.; Worobo, R. W.; Moraru, C. I. *Appl. Environ. Microbiol.* **2013**, *79*, 2703−2712.
(58) Iwata, F.; Shirasawa, T.; Mizutani, Y.; Ushiki, T. *Microscopy* **2021**, *70*, 423−435.
(59) Mortensen, N. P.; Fowlkes, J. D.; Sullivan, C. J.; Allison, D. P.; Larsen, N. B.; Molin, S.; Doktycz, M. J. *Langmuir* **2009**, *25*, 3728−3733.

https://doi.org/10.1021/acs.analchem.2c05303
Anal. Chem. XXXX, XXX, XXX−XXX